Article

Electronic Structure Calculation of Cr^{3+} and Fe^{3+} in Phosphor Host Materials Based on Relaxed Structures by Molecular Dynamics Simulation

Joichiro Ichikawa [1], Hiroko Kominami [2], Kazuhiko Hara [3], Masato Kakihana [4] and Yuta Matsushima [1,*]

[1] Chemistry and Chemical Engineering, Yamagata University, Yamagata 992-8510, Japan; ttk40581@st.yamagata-u.ac.jp
[2] Electronics and Materials Science, Shizuoka University, Shizuoka 432-8561, Japan; kominami.hiroko@shizuoka.ac.jp
[3] Research Institute of Electronics, Shizuoka University, Shizuoka 432-8011, Japan; hara.kazuhiko@shizuoka.ac.jp
[4] Institute of Scientific and Industrial Research, Osaka University, Osaka 567-0047, Japan; kakihana@sanken.osaka-u.ac.jp
[*] Correspondence: ymatsush@yz.yamagata-u.ac.jp; Tel.: +81-238-26-3165

Abstract: The electronic structures of the luminescent center ions Cr^{3+} and Fe^{3+} in the deep red phosphors $LiAl_5O_8$:Cr^{3+}, α-Al_2O_3:Cr^{3+}, and γ-$LiAlO_2$:Fe^{3+} were calculated by the DV-$X\alpha$ method, in which the local distortion induced by the replacement of Al^{3+} sites in the host crystals by the luminescent center ions was reproduced by classical molecular dynamics (MD) simulation. The MD simulations based on classical dynamics allowed for the handling of more than 1000 atoms for the lattice relaxation calculations, which was advantageous to simulate situations in which a small number of foreign atoms (ions) were dispersed in the host lattice as in phosphors, even when typical periodic boundary conditions were applied. The relaxed lattices obtained after MD indicated that the coordination polyhedra around Cr^{3+} and Fe^{3+} expanded in accordance with the size difference between the luminescent center ions and Al^{3+} in the host crystals. The overall profiles of the partial density of states (p-DOSs) of the isolated Cr^{3+} and Fe^{3+} 3d orbitals were not significantly affected by the lattice relaxation, whereas the widths of the energy splitting of the 3d orbitals were reduced. The electronic structure calculations for Fe–Fe pairs in γ-$LiAlO_2$ showed that the antiferromagnetic interactions with antiparallel electron spins between the Fe^{3+} ions were preferred, especially when the Fe–Fe pair was on the first-nearest neighboring cation sites.

Keywords: deep red phosphor; local distortion; electronic structure; molecular dynamics simulation; molecular orbital calculation

1. Introduction

Phosphors are materials that emit luminescence, usually in the visible range, when they are stimulated by high-energy radiation such as X-rays or ultraviolet (UV) rays, or by electron beams. Inorganic phosphors have been practically used in fluorescent lamps and cathode-ray tubes, and they are increasingly being applied to lighting applications using white LED lamps. Yttrium aluminum garnet (YAG) doped with Ce^{3+} is a conventional yellow phosphor excited by blue light emitted from LED chips, and SiAlON and $CaAlSiN_3$ doped with Eu^{2+} have recently been developed as phosphors that emit orange to red luminescence in white LED lamps [1–8].

Recently, we have focused on the 3d transition metals Cr^{3+}, Mn^{4+}, and Fe^{3+} as luminescent centers [9,10] since the emission exists in the deep red region, as in Mg_2TiO_4:Mn^{4+}, α-Al_2O_3:Cr^{3+}, $LiAl_5O_8$:Fe^{3+}, and γ-$LiAlO_2$:Fe^{3+}. Such deep red emission is difficult to achieve with rare earth phosphors, and their relatively sharp emission peaks are advantageous for improving color rendering in lighting applications.

This paper proposes a computational approach that combines classical MD simulations and molecular orbital (MO) calculations using the DV-Xα method in order to effectively investigate the electronic structures of luminescent ions in phosphors. The advantages of this approach are as follows.

(1) MD reproduces the local lattice distortion induced by substitution of foreign ions (in this case, luminescent center ions) prior to the electronic structure calculations. For example, γ-LiAlO$_2$:Fe^{3+} is a deep-red phosphor [9,11] in which Fe^{3+} replaces Al^{3+} in the host lattice. The ionic radii of Fe^{3+} and Al^{3+} in four-hold coordination are 0.49 Å and 0.39 Å, respectively [12], with the larger Fe^{3+} ion pushing the ligand oxygens away and expanding the coordination polyhedron. Such local distortion affects the electronic structure of the central Fe^{3+} according to the conventional crystal field theory.

MD can readily give a relaxed arrangement of the constituent atoms, even when two or more foreign ions or vacancies are introduced in a host lattice.

(2) With the development of computational techniques, ab-initio MDs such as CASTEP [13], VASP [14–17], and FMO-MD [18] have become available over the decades. In contrast to these ab-initio MDs, classical MDs describe atomic interactions between the constituent atoms by simple two-body potentials, allowing a larger number of atoms to be handled in the simulation with reasonable accuracy. It is suitable for simulating a dilute situation in which luminescent center ions are randomly dispersed in the lattice of the phosphor host crystal. Unexpected periodicity in the arrangement of luminescent center ions in the calculation cell, due to periodic boundary conditions often applied in MD simulations, can be avoided, as it can occur when the cell is constructed with a limited number of atoms.

A similar approach has been reported for glass materials to investigate the electronic structures of glass under strong electric fields [19], in which MD was effectively used to simulate the atomic arrangement, since structural analysis such as the X-ray diffraction technique is not applicable to glass. Quite limited research has attempted to reveal the effects of local distortion using a combination of classical MD and MO techniques in dilute systems such as phosphors. This work is a pioneering study applying this approach to crystalline materials, focusing on LiAl$_5$O$_8$:Cr^{3+}, α-Al$_2$O$_3$:Cr^{3+}, and γ-LiAlO$_2$:Fe^{3+} deep red phosphors.

Figure S1 shows the crystal structures of the host materials. LiAl$_5$O$_8$ has a spinel-type structure [20], with tetrahedral and octahedral sites for the cations, and Cr^{3+} is considered to replace Al^{3+} in the octahedral sites. Corundum-type α-Al$_2$O$_3$ has a crystal structure in which two AlO$_6$ octahedra share one face to form an Al$_2$O$_9$ dimer, providing octahedral sites for Cr^{3+} [21]. The crystal structure of γ-LiAlO$_2$ contains tetrahedra of AlO$_4$ and LiO$_4$ [22], offering tetrahedral sites for the luminescent center ion Fe^{3+}. Figure S2 shows the emission and excitation spectra of these deep red phosphors. Cr^{3+} shows sharp line spectra at 716 nm for LiAl$_5$O$_8$ and 694 nm for α-Al$_2$O$_3$, with two excitation bands around 420 nm and 570 nm due to the d-d transitions. Fe^{3+} in γ-LiAlO$_2$ shows a rather broad emission peak from 640 to 900 nm, with the peak top around 740 nm. The main excitation band of Fe^{3+} in the UV region around 240 nm is due to the charge transfer transition; the smaller excitation bands at 390 nm and 450 nm are due to the d-d transitions.

The objective of this work is to demonstrate the effectiveness and potential of our combined MD and MO approach to elucidate the effect of lattice relaxation on the electronic structures of the luminescent center ions in the host lattices. This approach will lead to a better understanding of phosphor materials and to help in developing materials with better properties.

2. Methods

2.1. Molecular Dynamics (MD) Simulation

MD simulations were carried out using the MXDORTO code [23]. The interaction between the constituent atoms was described by the Born–Mayer–Huggins type pair potential (Equation (1)).

$$U_{ij} = \frac{Z_i Z_j e^2}{r_{ij}} + A_{ij}\, exp\left(-\frac{r_{ij}}{\rho_{ij}}\right) \tag{1}$$

In Equation (1), U_{ij} is the potential of a pair of atoms i and j, and z_i and z_j are the oxidation numbers of ions i and j, respectively. The constituent atoms were assumed to be fully ionized; Al, Cr, and Fe were assumed to be +3, Li +1, and O −2. e is the electron charge, and r_{ij} is the atomic distance between ions i and j. The first term represents the electronic interaction between ions i and j, and A_{ij} and ρ_{ij} in the second term are potential parameters that determine the short-range repulsive interaction. These potential parameters were refined to reproduce the reference crystal structures of α-Al_2O_3 [21], Li_2O [24], α-$LiAlO_2$ [25], γ-$LiAlO_2$ [22], $LiAl_5O_8$ [20], Cr_2O_3 [26], $LiCrO_2$ [27], Fe_2O_3 [28], and $LiFe_5O_8$ [29] with agreement within 2% of the lattice parameters in the NPT ensemble (N: number of atoms, P: pressure, and T: temperature) at 300 K (Table S1). The potential parameters A_{ij} and ρ_{ij} are listed in Table 1. Table S1 shows the coincidence between the simulated and reference crystal structures with respect to the lattice parameters and the mean square displacement (MSD) of the constituent atoms in MD. The MSD was comparable to the magnitude of typical thermal vibrations. It should be noted that a single set of the potential parameters for each atom pair reproduced the reference crystal structures properly, even though both octahedral and tetrahedral coordination sites exist for Li^+, Al^{3+}, and Fe^{3+} (only octahedral for Cr^{3+}) in the reference crystals.

Table 1. Potential parameters, A_{ij} and ρ_{ij}, used in this work. Short-range repulsion was not considered for the cation pairs except Li–Li.

Atom Pair	A_{ij} (eV)	ρ_{ij} (Å)
O–O	1997.28	0.2810
Al–O	1716.41	0.2810
Li–O	960.0	0.2690
Li–Li	98.9357	0.2994
Cr–O	1156.68	0.3131
Fe–O	1200.68	0.3151

The initial atomic arrangement of each host crystal was obtained from the crystal structure reported in the literature [20–22]. The orthogonal MD cells were constructed by repeating the crystallographic unit cells with x, y, and z axes of 23–26 Å and contained 1512, 1800, and 1600 atoms for $LiAl_5O_8$, α-Al_2O_3, and γ-$LiAlO_2$, respectively. The periodic boundary conditions were applied to the calculations. Cr^{3+} and Fe^{3+} ions were introduced in the MD cells by substituting Al^{3+} sites according to the following conditions.

1. To investigate the effect of lattice relaxation for the isolated luminescent center ion, one Cr^{3+} ion was introduced to replace the Al^{3+} on the octahedral site in $LiAl_5O_8$ and α-Al_2O_3; in γ-$LiAlO_2$, the Al^{3+} on the tetrahedral site was replaced by one Fe^{3+} ion.
2. To investigate the interaction between Fe–Fe pairs in γ-$LiAlO_2$, two Fe^{3+} ions were placed at the first-, second-, and third-nearest neighboring Al^{3+} positions.

The initial structures were relaxed for 1000 steps at 300 K with a time step of 2 fs in the NVT ensemble (V: volume), and for 3000 steps in the NPT ensemble. The temperature of the systems was then increased to 1500 K at a ramp rate of 0.1 K/step in the NPT ensemble and maintained at 1500 K for 100,000 steps. The systems were cooled to 300 K at a ramp rate of −0.1 K/step and relaxed for 31,000 steps at 300 K. The relaxed positions of the constituent atoms were obtained by averaging the atomic coordinates of the last 1000 steps.

The coordination environments around the cations were discussed using the frequency distribution (FD) corresponding to the number of focusing atoms surrounding the central atom in the thin shell at a distance R with a width of ΔR (here 0.01 Å).

2.2. Molecular Orbital (MO) Calculations

The electronic structures of the luminescent center ions of Cr^{3+} and Fe^{3+} were calculated by the DV-Xα method using the DVSCAT code [30,31], where the relativistic effects were not taken into account. The calculation clusters for MO were extracted from the relaxed structurers obtained by the MD simulations. The clusters were arranged with Cr^{3+} or Fe^{3+} at the centers, with Al and Li octahedra or tetrahedra surrounding the central CrO_6 or FeO_4. The clusters used in the MO calculations are shown in Table 2 and Figures S3 and S4.
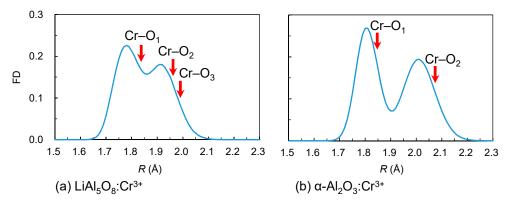
Table 2. Clusters for molecular orbital calculations.

Luminescent Center	Host Crystal	Calculation Cluster
Cr^{3+} (octahedral)	$LiAl_5O_8$ α-Al_2O_3	$(Li_2Al_{10}CrO_{38})^{41-}$ $(Al_{13}CrO_{45})^{48-}$
Fe^{3+} (tetrahedral)	γ-$LiAlO_2$	$(Li_9Al_6FeO_{32})^{34-}$ for isolated Fe^{3+} $(Li_9Al_5Fe_2O_{32})^{34-}$ for Fe^{3+}–Fe^{3+} interaction at the first- and second-nearest neighbors $(Li_9Al_6Fe_2O_{34})^{35-}$ for Fe^{3+}–Fe^{3+} interaction at the third-nearest neighbor

The calculation clusters were embedded in the Madelung potential generated by the Evjen method [32], and atoms outside the clusters were treated as point charges placed at the positions obtained by MD. The spin polarization was taken into account in the MO calculations, and both Cr^{3+} and Fe^{3+} were started in the high-spin states.

3. Results and Discussion

3.1. Electronic Structures of Isolated Cr^{3+}

Figure 1 shows the averaged FDs of O atoms around Al in $LiAl_5O_8$:Cr^{3+} (a) and α-Al_2O_3:Cr^{3+} (b). Spinel-type $LiAl_5O_8$ contains tetrahedral and octahedral sites for Al^{3+}. The crystallographic data of $LiAl_5O_8$ [20] provide 1.779 Å $\times$ 3, 1.835 Å $\times$ 1 for the A–O distances at the tetrahedral site and 1.856 Å $\times$ 2, 1.905 Å $\times$ 2, and 1.940 Å $\times$ 2 for the octahedral site. The corundum structure of α-Al_2O_3 consists of AlO_6 octahedra forming face-sharing Al_2O_9 dimers (Figure S1), with Al^{3+} at the octahedral off-center position and the Al–O distances of 1.857 Å $\times$ 3 and 1.970 Å $\times$ 3 [21].
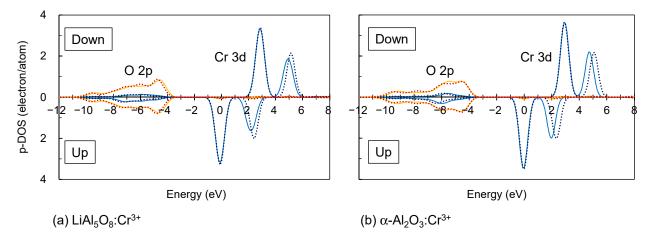

Figure 1. Frequency distributions of O atoms around Al for (**a**,**b**). The arrows indicate the Cr–O distances obtained by MD.

The lattice relaxation by MD resulted in bimodal Al–O distribution with peak tops at around 1.78 Å and 1.91 Å for $LiAl_5O_8$:Cr^{3+} (a) and 1.80 Å and 2.00 Å for α-Al_2O_3:Cr^{3+} (b), as shown Figure 1. The red arrows in Figure 1 indicate the Cr–O distances obtained

by MD: 1.84 Å × 2 (Cr–O_1), 1.96 Å × 2 (Cr–O_2), and 1.99 Å × 2 (Cr–O_3) for $LiAl_5O_8$:Cr^{3+} (a), and 1.85 Å × 3 (Cr–O_1) and 2.07 Å × 3 (Cr–O_2) for α-Al_2O_3:Cr^{3+} (b). The arrows are on the longer sides of the Al–O peaks, indicating that the larger Cr^{3+} ions expanded the CrO_6 octahedron compared to AlO_6. The MD results showed that the Cr^{3+} in the $AlCrO_9$ dimer in α-Al_2O_3:Cr^{3+} was displaced by 0.06 Å toward the octahedral void compared to the position of Al^{3+} in the Al_2O_9 dimer, which was consistent with ~0.1 Å estimated in the crystal field calculations for α-Al_2O_3:Cr^{3+} [33].

Figure 2 shows the partial density of states (p-DOSs) of Cr 3d and O 2p orbitals in $LiAl_5O_8$:Cr^{3+} (a) and α-Al_2O_3:Cr^{3+} (b), calculated based on the lattice relaxed by MD (solid line) and the unrelaxed lattice without MD (dotted line), where the HOMO levels are set at 0 eV. Figure 2 shows that the 3d orbitals of Cr^{3+} were divided into two groups, and that Cr^{3+} preferred the high-spin state regardless of the host material or lattice relaxation. These basic features were consistent with the considerations based on the conventional crystal field theory for Cr^{3+} in the octahedral symmetry.

(a) $LiAl_5O_8$:Cr^{3+} (b) α-Al_2O_3:Cr^{3+}

Figure 2. Partial density of states of Cr 3d and O 2p orbitals in (**a**,**b**) with the HOMO levels set at 0 eV. The profiles were drawn with a Gaussian width of 0.3 eV. Solid line: p-DOSs for the relaxed lattice after MD, dotted line: p-DOSs for the unrelaxed lattice without MD.
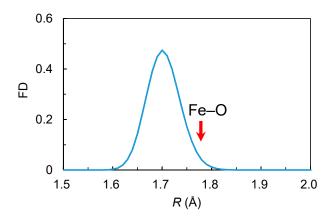
The CrO_6 octahedra were not in the ideal octahedral symmetry (O_h) even without relaxation, but for ease of understanding, the conventional notations t_{2g} and e_g are used to represent the split d orbitals. The HOMO level is in the t_{2g} orbitals, reflecting the d^3 configuration of Cr^{3+}. Hybridization of Cr 3d and O 2p was found to be limited, with the O 2p and Cr 3d contributions observed separately at −10 to −4 eV and −1 to 6 eV, respectively.

The lattice relaxation by MD did not significantly affect the overall profiles of the p-DOSs, but the d-orbital splitting between t_{2g} and e_g orbitals of Cr 3d decreased from 2.52 eV to 2.30 eV in $LiAl_5O_8$ and from 2.37 eV to 2.01 eV in α-Al_2O_3 due to the lattice relaxation, reflecting a reduction in the ligand field strength due to the expansion of the coordination polyhedra.
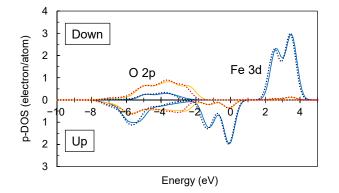
3.2. Electronic Structures of Fe^{3+}

3.2.1. Isolated Fe^{3+}

Figure 3 shows the FD of Al–O in γ-$LiAlO_2$:Fe^{3+} obtained by MD. The averaged Fe–O distance is on the longer side of the Al–O peak, indicating that the FeO_4 tetrahedron expanded due to the size difference between Fe^{3+} and Al^{3+}.

Figure 3. Frequency distribution of O atoms around Al in γ-LiAlO$_2$:Fe^{3+}. The red arrow indicates the averaged Fe–O distance observed in the relaxed structure after MD.

Figure 4 plots the p-DOSs of Fe 3d and O 2p orbitals for the lattices with MD (solid line) and without MD (dotted line), with the HOMO levels set at 0 eV. Fe^{3+} in the d^5 configuration converged to the high-spin state with two groups of the d orbitals. Although the FeO$_4$ tetrahedron was not in the ideal tetrahedral symmetry (T_d), the conventional notations t_2 and e are used as discussed for Cr^{3+} above. The HOMO level is in the t_2 orbital. The lattice relaxation by MD did not significantly affect the overall profile of the p-DOS as in the case of Cr^{3+} (Figure 4), but it did reduce the energy splitting between the t_2 and e orbitals from 1.22 eV (dotted line) to 1.17 eV (solid line).
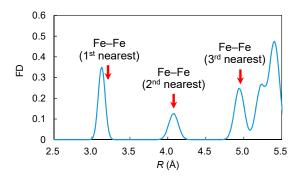

Figure 4. Partial density of states of Fe 3d and O 2p orbitals in γ-LiAlO$_2$:Fe^{3+} with the HOMO level set at 0 eV. The profiles were drawn with the Gaussian width of 0.3 eV. Solid line: p-DOSs for the relaxed lattice after MD, dotted line: p-DOSs for the unrelaxed lattice without MD.

The MO calculations show that the Fe 3d orbitals were highly hybridized with O 2p, which was more pronounced for the up-spin electrons. From −8 to −3 eV, the large contribution of Fe 3d was recognized along with O 2p, while from −2 to 1 eV, the contribution of O 2p was observed along with Fe 3d.

3.2.2. Fe^{3+}–Fe^{3+} Interaction

To investigate the magnetic interactions between the Fe–Fe pairs, the additional Fe^{3+} was placed on the first-, second-, and third-nearest neighboring Al^{3+} sites from the central Fe^{3+} (Figure S4). Figure S4 shows the clusters for the MO calculations for the Fe–Fe pairs.
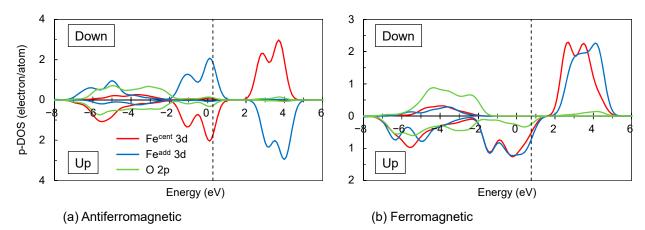
Figure 5 shows the FD of Al–Al. The arrows on the figure indicate the distances of Fe–Fe pairs on the first-, second-, and third-nearest neighboring Al^{3+} sites.

Figure 5. Frequency distribution of Al atoms around Al in γ-LiAlO$_2$:Fe^{3+}. The arrows indicate the Fe–Fe distances observed in the relaxed structures after MD.

Compared to the Al–Al distances, the distance between the first-nearest Fe–Fe pair was elongated, and the distances between the second- and third-nearest Fe–Fe pairs were almost the same as the corresponding Al–Al distance. It indicated that the effect of the size difference between Al^{3+} and Fe^{3+} was probably counteracted by the connection angles between the point-sharing Al(Fe)O$_4$ tetrahedra.

Figure 6 shows the p-DOSs of the Fe 3d and O 2p orbitals for the first-nearest Fe–Fe pair. The second- and third-nearest Fe–Fe pairs yielded the p-DOSs with substantially the same features as in Figure 6. The initial ferromagnetic and antiferromagnetic configurations converged to their respective configurations. To compare the relative stability of the systems with the different magnetic configurations, the HOMO levels of the p-DOSs were not set at 0 eV; the HOMO levels were indicated by the dashed lines. Table 3 compares the HOMO energies obtained for the different magnetic configurations. It should be noted here that the comparison should be limited to within the same calculation cluster, since the calculated energy is also influenced by the cluster type itself. Table 3 shows that the antiferromagnetic interaction was favored by 0.49 eV, 0.02 eV, and 0.05 eV for the Fe–Fe pairs at the first-, second-, and third-nearest neighboring positions, and the stabilizing effect of the antiferromagnetic interaction was particularly pronounced for the first nearest Fe–Fe pair. Such magnetic interaction was considered to be related to the well-known "superexchange interaction" often observed in compounds containing magnetically active cations [34–36]. Fe^{3+}–O^{2-}–Fe^{3+} in Figure S4a was about 130°, intermediate between 90° and 180°. The magnetic interaction between Fe^{3+} occupying tetrahedral sites have rarely been reported in the literature, whereas for Fe^{3+} in octahedral sites, the antiferromagnetic interaction have been reported, for example, in spinel-type ZnFe$_2$O$_4$ and colundum-type Fe$_2$O$_3$ with the Neel temperatures of ~10 K and 950 K, respectively.

(a) Antiferromagnetic

(b) Ferromagnetic

Figure 6. Partial density of states of the Fe 3d and O 2p orbitals in γ-LiAlO$_2$:Fe^{3+}. The dashed lines indicate the HOMO energies. The profiles were drawn with the Gaussian width of 0.3 eV. Fe^{cent}: Fe atom at the center, Fe^{add}: additional Fe atom.

Table 3. Difference in the HOMO energies between antiferromagnetic and ferromagnetic configurations in the Fe–Fe pairs.

	HOMO Energy (eV)		Energy Difference (eV)
	Antiferromagnetic	**Ferromagnetic**	**Anti.−Ferro.**
Nearest	0.27	0.76	−0.49
Second nearest	0.30	0.32	−0.02
Third nearest	0.18	0.23	−0.05

4. Conclusions

This work demonstrated the MO calculations of the electronic structures of the luminescent center ions Cr^{3+} and Fe^{3+} introduced in the host lattices $LiAl_5O_8$, α-Al_2O_3, and γ-$LiAlO_2$. The local distortions induced by replacing the smaller Al sites were reproduced by the MD simulations based on the classical dynamics. For the isolated Cr^{3+} and Fe^{3+} in these host crystals, the MD simulations confirmed the expansion of the coordination polyhedra around these cations. The MO calculations showed that these luminescent center ions preferred the high-spin states, and that the lattice relaxation by MD reduced the energy splitting of the d orbitals between t_{2g} and e_g for Cr^{3+} on the octahedral site and t_2 and e for Fe^{3+} on the tetrahedral site. Without the lattice relaxation by MD, the energy splitting was overestimated by about 10% for $LiAl_5O_8$:Cr^{3+}, 20% for α-Al_2O_3:Cr^{3+}, and 4% for γ-$LiAlO_2$:Fe^{3+}. The MD simulations also indicated that the paired Fe^{3+} ions in γ-$LiAlO_2$:Fe^{3+} shifted away from each other, which was more pronounced for the first-nearest neighboring pair. The Fe–Fe pairs preferred the antiferromagnetic interactions, and the degree of the stabilization of the antiparallel orientation of the d^5 electrons was found to be maximal at about 0.5 eV for the first-neighboring Fe–Fe pair.

Supplementary Materials: The following are available online at https://www.mdpi.com/article/10.3390/technologies10030056/s1, Table S1. Comparison of the lattice parameters simulated by MD using the potential parameters (A_{ij} and ρ_{ij}) in Table 1 with those experimentally determined (Exp.), [37]. Figure S1: Crystal structures of (a) $LiAl_5O_8$, (b) α-Al_2O_3, and (c) γ-$LiAlO_2$, Figure S2: Emission and excitation spectra of (a) $LiAl_5O_8$:Cr^{3+}, (b) α-Al_2O_3:Cr^{3+}, and (c) γ-$LiAlO_2$:Fe^{3+}, Figure S3: Calculation clusters for isolated Cr^{3+} and Fe^{3+} in (a) $LiAl_5O_8$:Cr^{3+} [$(Li_2Al_{10}CrO_{38})^{41-}$], (b) α-Al_2O_3:Cr^{3+} [$(Al_{13}CrO_{45})^{48-}$], and (c) γ-$LiAlO_2$:Fe^{3+} [$(Li_9Al_6FeO_{32})^{34-}$], Figure S4: The clusters for the calculation of the electronic interaction in the Fe–Fe pairs on (a) first-, (b) second-, and (c) third-nearest cation sites.

Author Contributions: Conceptualization, Y.M.; methodology, J.I. and Y.M.; software, J.I. and Y.M.; validation, H.K., K.H., M.K. and Y.M.; formal analysis, J.I. and Y.M.; investigation, J.I.; resources, Y.M.; data curation, J.I. and Y.M.; writing—original draft preparation, J.I. and Y.M.; writing—review and editing, H.K., K.H., M.K. and Y.M.; visualization, J.I. and Y.M.; supervision, Y.M.; project administration, Y.M.; funding acquisition, K.H., M.K. and Y.M. All authors have read and agreed to the published version of the manuscript.

Institutional Review Board Statement: Not applicable.

Informed Consent Statement: Not applicable.

Data Availability Statement: Not applicable.

Conflicts of Interest: The authors declare no conflict of interest. The funders had no role in the design of the study; in the collection, analyses, or interpretation of data; in the writing of the manuscript, or in the decision to publish the results.

References

1. Xie, R.-J.; Mitomo, M.; Uheda, K.; Xu, F.F.; Akimune, Y. Preparation and luminescence spectra of calcium- and rare-earth (R = Eu, Tb, and Pr)-codoped α-SiAlON ceramics. *J. Am. Ceram. Soc.* **2002**, *85*, 1229–1234. [CrossRef]

2. van Krevel, J.W.H.; van Rutten, J.W.T.; Mandal, H.; Hintzen, H.T.; Metselaar, R. Luminescence properties of terbium-, cerium-, or europium-doped α-sialon materials. *J. Solid State Chem.* **2002**, *165*, 19–24. [CrossRef]

3. Xie, R.-J.; Hirosaki, N.; Sakuma, K.; Yamamoto, Y.; Mitomo, M. Eu^{2+}-doped Ca-α-SiAlON: A yellow phosphor for white light-emitting diodes. *Appl. Phys. Lett.* **2004**, *84*, 5404–5406. [CrossRef]

4. Sakuma, K.; Omichi, K.; Kimura, N.; Ohashi, M.; Tanaka, D.; Hirosaki, N.; Yamamoto, Y.; Xie, R.-J.; Suehiro, T. Warm-white light-emitting diode with yellowish orange SiAlON ceramic phosphor. *Opt. Lett.* **2004**, *29*, 2001–2003. [CrossRef]

5. Xie, R.-J.; Hirosaki, N.; Mitomo, M.; Yamamoto, Y.; Suehiro, T.; Sakuma, K. Optical properties of Eu^{2+} in α-SiAlON. *J. Phys. Chem. B* **2004**, *108*, 12027–12031. [CrossRef]

6. Uheda, K.; Hirosaki, N.; Yamamoto, H. Host lattice materials in the system Ca_3N_2–AlN–Si_3N_4 for white light emitting diode. *Phys. Status Solidi A* **2006**, *203*, 2712–2717. [CrossRef]

7. Uheda, K.; Hirosaki, N.; Yamamoto, Y.; Naito, A.; Nakajima, T.; Yamamoto, H. Luminescence properties of a red phosphor, $CaAlSiN_3$: Eu^{2+}, for white light-emitting diodes. *Electrochem. Solid-State Lett.* **2006**, *9*, H22–H25. [CrossRef]

8. Watanabe, H.; Wada, H.; Seki, K.; Itou, M.; Kijima, N. Synthetic method and luminescence properties of $Sr_xCa_{1-x}AlSiN_3$:Eu^{2+} mixed nitride phosphors. *J. Electrochem. Soc.* **2008**, *155*, F31–F36. [CrossRef]

9. Takahashi, H.; Takahashi, H.; Watanabe, K.; Kominami, H.; Hara, K.; Matsushima, Y. Fe^{3+} red phosphors based on lithium aluminates and an aluminum lithium oxyfluoride prepared from LiF as the Li Source. *J. Lumin.* **2017**, *182*, 53–58. [CrossRef]

10. Kobayashi, R.; Tamura, H.; Kamada, Y.; Kakihana, M.; Matsushima, Y. A new host compound of aluminum lithium fluoride oxide for deep red phosphors based on Mn^{4+}, Fe^{3+}, and Cr^{3+}. *ECS Trans.* **2018**, *88*, 225–236. [CrossRef]

11. Aoyama, M.; Amano, Y.; Inoue, K.; Honda, S.; Hashimoto, S.; Iwamoto, Y. Synthesis and characterization of lithium aluminate red phosphors. *J. Lumin.* **2013**, *135*, 211–215. [CrossRef]

12. Shannon, R.D. Revised effective ionic radii and systematic studies of interatomic distances in halides and chalcogenides. *Acta Crystallogr. A* **1976**, *32*, 751–767. [CrossRef]

13. Clark, S.J.; Segall, M.D.; Pickard, C.J.; Hasnip, P.J.; Probert, M.I.J.; Refson, K.; Payne, M.C. First principles methods using CASTEP. *Z. Kristallogr.* **2005**, *220*, 567–570. [CrossRef]

14. Kresse, G.; Hafner, J. *Ab initio* molecular dynamics for liquid metals. *Phys. Rev. B* **1993**, *47*, 558–561. [CrossRef] [PubMed]

15. Kresse, G.; Hafner, J. *Ab initio* molecular-dynamics simulation of the liquid-metal-amorphous-semiconductor transition in germanium. *Phys. Rev. B* **1994**, *49*, 14251–14269. [CrossRef]

16. Kresse, G.; Furthmüller, J. Efficiency of *ab-initio* total energy calculations for metals and semiconductors using a plane-wave basis set. *Comput. Mat. Sci.* **1996**, *6*, 15–50. [CrossRef]

17. Kresse, G.; Furthmüller, J. Efficient iterative schemes for *ab initio* total-energy calculations using a plane-wave basis set. *Phys. Rev. B* **1996**, *54*, 11169–11186. [CrossRef]

18. Komeiji, Y.; Mochizuki, Y.; Nakano, T.; Mori, H. Recent advances in fragment molecular orbital-based molecular dynamics (FMO-MD) simulations. In *Molecular Dynamics—Theoretical Developments and Applications in Nanotechnology and Energy*; Wang, L., Ed.; InTech: London, UK, 2012. Available online: https://www.intechopen.com/chapters/34975 (accessed on 22 April 2022).

19. Makino, Y.; Tanaka, I.; Kawamura, K.; Adachi, H.; Hirao, K. Electronic structure of silica glass under strong electric field. *Prog. Theo. Phys. Suppl.* **2000**, *138*, 239–240. [CrossRef]

20. Famery, R.; Queyroux, F.; Gilles, J.-C.; Herpin, P. Etude structurale de la forme ordonnée de $LiAl_5O_8$. *J. Solid State Chem.* **1979**, *30*, 257–263. [CrossRef]

21. Ishizawa, N.; Miyata, T.; Minato, I.; Marumo, F.; Iwai, S. A structural investigation of α-Al_2O_3 at 2170 K. *Acta Crystallogr. B* **1980**, *36*, 228–230. [CrossRef]

22. Marezio, M. The crystal structure and anomalous dispersion of γ-$LiAlO_2$. *Acta Crystallogr.* **1965**, *19*, 396–400. [CrossRef]

23. Kawamura, K. Environmental Nano-Mechanics Molecular Simulations. Available online: https://kats-labo.jimdofree.com/mxdorto-mxdtricl/ (accessed on 5 March 2022).

24. Farley, T.W.D.; Hayes, W.; Hull, S.; Hutchings, M.T.; Vrtis, M. Investigation of thermally induced Li^+ ion disorder in Li_2O using neutron diffraction. *J. Phys. Condens. Matter* **1991**, *3*, 4761–4781. [CrossRef]

25. Marezio, M.; Remeika, J.P. High-pressure synthesis and crystal structure of α-$LiAlO_2$. *J. Chem. Phys.* **1966**, *44*, 3143–3145. [CrossRef]

26. Finger, L.W.; Hazen, R.M. Crystal structure and isothermal compression of Fe_2O_3, Cr_2O_3, and V_2O_3 to 50 kbars. *J. Appl. Phys.* **1980**, *51*, 5362–5367. [CrossRef]

27. Lu, Z.; Dahn, J.R. Structure and electrochemistry of layered $Li[Cr_xLi_{(1/3-x/3)}Mn_{(2/3-2x/3)}]O_2$. *J. Electrochem. Soc.* **2002**, *149*, A1454–A1459. [CrossRef]

28. Maslen, E.N.; Strel'tsov, V.A.; Strel'tsova, N.R.; Ishizawa, N. Synchrotron X-ray study of the electron density in α-Fe_2O_3. *Acta Crystallogr. B* **1994**, *50*, 435–441. [CrossRef]

29. Marin, S.J.; O'Keefe, M.; Partin, D.E. Structures and crystal chemistry of ordered spinels: $LiFe_5O_8$, $LiZnNbO_4$, and Zn_2TiO_4. *J. Solid State Chem.* **1994**, *113*, 413–419. [CrossRef]

30.　Adachi, H.; Tsukada, M.; Satoko, C. Discrete variational Xα cluster calculations. I. Application to metal clusters. *J. Phys. Soc. Jpn.* **1978**, *45*, 875–883. [CrossRef]

31.　Ellis, D.E.; Painter, G.S. Discrete variational method for the energy-band problem with general crystal potentials. *Phys. Rev. B* **1970**, *2*, 2887–2898. [CrossRef]

32.　Evjen, H.M. On the stability of certain heteropolar crystals. *Phys. Rev.* **1932**, *39*, 675–687. [CrossRef]

33.　McClure, D.S. Optical spectra of transition-metal ions in corundum. *J. Chem. Phys.* **1962**, *36*, 2757–2779. [CrossRef]

34.　Anderson, P.W. Antiferromagnetism. Theory of superexchange interaction. *Phys. Rev.* **1950**, *79*, 350–356. [CrossRef]

35.　Kanamori, J. Superexchange interaction and symmetry properties of electron orbitals. *J. Phys. Chem. Solids* **1959**, *10*, 87–98. [CrossRef]

36.　Yamashita, J.; Kondo, J. Superexchange interaction. *Phys. Rev.* **1958**, *109*, 730–741. [CrossRef]

37.　Momma, K.; Izumi, F. VESTA 3 for three-dimensional visualization of crystal, volumetric and morphology data. *J. Appl. Crystallogr.* **2011**, *44*, 1272–1276. [CrossRef]